



Single-particle states in ^{59}Ni with $^{58}\text{Ni}(\vec{d}, p)^{59}\text{Ni}$ reaction at 56 MeV and neutron-bound-state complex potentials

O. Iwamoto ^a, A. Nohtomi ^a, Y. Uozumi ^a, T. Sakae ^a, M. Matoba ^a,
M. Nakano ^b, T. Maki ^b, N. Koori ^c

^a *Department of Nuclear Engineering, Kyushu University, Fukuoka 812, Japan*

^b *School of Nursing and Technology, University of Occupational and Environmental Health, Kitakyushu 807, Japan*

^c *Faculty of Integrated Arts and Sciences, Tokushima University, Tokushima 770, Japan*

Received 17 March 1994

Abstract

Angular distributions of the cross sections and analyzing powers were measured for the $^{58}\text{Ni}(d,p)^{59}\text{Ni}$ reaction up to the excitation energy of 10 MeV in ^{59}Ni with a high-resolution polarized deuteron beam at 56 MeV. Spins and parities were assigned for 33 discrete levels up to the excitation energy of 8 MeV. Spectroscopic factors, single-particle energies and spreading widths of $1f_{5/2}$, $2p_{3/2}$, $2p_{1/2}$, $1g_{9/2}$ states were obtained. Neutron-bound-state complex potentials have been calculated from the resultant spreading widths and energies together with results from other one-nucleon transfer-reaction experiments on nickel and calcium isotopes. It is found that the energy dependence of the spreading widths of the single-particle and -hole states and then the imaginary parts of the bound-state potentials in the excitation energy region of 0–10 MeV show a symmetrical behavior with respect to the Fermi surface.

Key words: NUCLEAR REACTIONS $^{58}\text{Ni}(\text{polarized } d, p)$, $E = 56$ MeV; measured $\sigma(\theta)$, analyzing power. ^{59}Ni levels deduced, spectroscopic factor, spreading width, neutron-bound-state complex potential

1. Introduction

Many spectroscopic experiments have been performed for nickel isotopes to study the nuclear structure based on the shell model. A number of large-scale

calculations with shell models are published up to now for p-f-shell nuclei, and detailed comparisons with experiments have been performed. The spectroscopy on ^{58}Ni is of particular interest in the nickel isotopes because of the proximity of the doubly-magic nucleus ^{56}Ni . A one-nucleon transfer reaction is one of the useful tools to study the single-particle or -hole picture in nuclei. Most of the early experiments, however, were performed using unpolarized beams that made ambiguous spin assignments of the transferred nucleon. The (d, p) reactions on ^{58}Ni with unpolarized beams were measured by Fulmer et al. [1] at 12 MeV, by Cosman et al. [2] at 7 MeV, by Chowdhury and Sen Gupta [3] at 10 MeV. Though their experiments were performed with very high resolution, only orbital angular momenta were definitely determined. Total angular momenta were determined by comparison with other experiments and considerations based on the shell-model energy systematics. Chowdhury and Sen Gupta performed j -assignments for the negative-parity states by the detailed study on j -dependent features of the angular distribution of the cross section, but some ambiguities of j -assignments for the positive-parity states and the weakly excited negative-parity states have been remained. The (d, p) reaction experiments with polarized beams were performed by Aymar et al. [4] at 10 MeV (1973) and Taylor et al. [5] at 10 MeV (1980), but their analyses were restricted to a few low-lying excited states.

Recently an approach with the dispersion relation to the optical-model potential and the shell-model potential has been studied theoretically by Mahaux et al. [6]. While the real part of the shell-model potential is evaluated to reproduce the single-particle or -hole state energy, the imaginary part of the shell-model potential is deduced from the spreading width of the fragmentation of the single-particle and -hole states. Some of the present authors reported fragmentations of neutron-hole states in medium-weight nuclei [7–12]. Mairle et al. reported global properties of proton-hole states for several medium-weight nuclei [13]. Further experimental studies on the spreading width from one-nucleon transfer reactions, especially stripping reactions, are desired for the evaluation of the imaginary part of the nucleon potential in the energy region between the Fermi surface and the zero energy.

Our group has studied neutron-particle and -hole states systematically in several medium-weight nuclei with one-nucleon transfer reactions using a high-resolution polarized beam [10–12]. In the present work, we report results of the neutron-particle states with the $^{58}\text{Ni}(d, p)^{59}\text{Ni}$ reaction measured at the Research Center for Nuclear Physics (RCNP), Osaka University, in which an AVF cyclotron with a polarized ion source and a high-resolution magnetic spectrograph have been installed. In this paper, the experimental procedure and the theoretical analysis of the angular distribution are described in sect. 2. The results of the experiment and the analysis are described with the table of the obtained angular momenta and spectroscopic factors in sect. 3. Integrated properties of single-particle states and bound-state complex potentials are evaluated and discussed in sect. 4. The results are summarized in sect. 5. The preliminary results of this work were reported in the RCNP annual report [14] and at a conference [15].

2. Experiment and data analysis

2.1. Experimental procedure

The experiment was carried out at the AVF cyclotron facility of RCNP, Osaka University. A polarized deuteron beam of 56 MeV energy was momentum-analyzed and bombarded a 99.89% enriched ^{58}Ni target of thickness 0.473 mg/cm^2 . The Average polarization of the deuteron beam was about 50%, which was monitored every 90 seconds throughout the experiment. Emitted protons were analyzed with the magnetic spectrograph RAIDEN [16] viewed with the focal-plane detector system KYUSHYU [17]. Angular distributions of the cross sections and analyzing powers were measured at 5° – 45° laboratory angles. The measured excitation energy region is 0–10 MeV. The normalization of the absolute cross section has been performed by scaling the $^{58}\text{Ni}(\text{d}, \text{d})$ elastic-scattering cross section, measured with the same target and optics, to an optical-model prediction using parameters of Matsuoka et al. [18]. The accuracy of the normalization is estimated to be better than 10%, which is mainly due to the ambiguity of the procedure for fitting the theoretical to the experimental angular distributions. The errors attributed to run-to-run variations of the integrated beam current are on the order of a few percent. The obtained normalization factor has been checked with the results estimated from the standard target-weight and solid-angle measurement. The details of the experimental method are described in previous works [7–10].

2.2. Data analysis

The cross-section and analyzing-power data were analyzed with the distorted-wave Born approximation (DWBA) code DWUCK [19] under the zero-range local-energy approximation model. It has been known that the conventional

Table 1

The optical-potential parameters used in the DWBA calculations for the $^{58}\text{Ni}(\text{d}, \text{p})^{59}\text{Ni}$ reaction at 56 MeV^f

| Particle | V (MeV) | r (fm) | a (fm) | r_c (fm) | W_v (MeV) | W_s (MeV) | r' (fm) | a' (fm) | V_{so} (MeV) | r_{so} (fm) | a_{so} (fm) |
|----------|--------------|-------------|-------------|----------------|----------------|----------------|--------------|--------------|-------------------|------------------|------------------|
| deuteron | 95.27 | 1.70 | 0.78 | 1.30 | 8.06 | 10.80 | 1.29 | 0.59 | 6.20 | 1.06 | 0.75 |
| proton | ^a | 1.16 | 0.75 | 1.30 | ^b | ^c | 1.37 | ^d | 6.04 | 1.06 | 0.78 |
| neutron | ^e | 1.25 | 0.65 | $\lambda = 25$ | | | | | | | |

^a $V = 49.9 - 0.22 E_p + 26.4 (N - Z)/A + 0.4 Z/A^{1/3}$.

^b $W_v = 1.2 + 0.09 E_p$.

^c $W_s = 4.2 - 0.05 E_p + 15.5 (N - Z)/A$.

^d $a' = 0.74 - 0.008 E_p + (N - Z)/A$.

^e Adjusted to reproduce the separation energy.

^f Nonlocality parameter $\beta_d = 0.54$ for deuterons, $\beta_p = 0.85$ for protons, and $\beta_n = 0.85$ for neutrons. Finite-range parameter = 0.621.

calculation with best-fit optical potentials in the proton and deuteron channels does not reproduce the shape of the angular distribution of the cross section for (d, p) reactions well at medium energies, but the use of an adiabatic potential [20] for the deuteron channel improves the overall fitting of the data considerably. The optical-potential parameters for deuterons were constructed with the proton and neutron global-potential parameters of Becchetti and Greenlees [21], and for protons the global-potential parameters of Menet et al. [22] were used. The used parameter sets with definition of a standard form are listed in Table 1. The neutron-bound-state wave functions were calculated in an Woods–Saxon well with the standard geometrical parameters, $r_0 = 1.25$ fm and $a_0 = 0.65$ fm and a Thomas spin–orbit term with the $\lambda = 25$ factor [19]. The well depth was adjusted to reproduce the neutron-separation energy.

In the local-energy approximation model of DWBA, the parameter of the finite-range effect 0.692 was used and parameters of the nonlocality effects for neutron, proton and deuteron potentials, $\beta_n = 0.85$, $\beta_p = 0.85$, and $\beta_d = 0.54$, respectively, were adopted. The spectroscopic factor via the (d, p) reaction is obtained with the equation

$$\frac{d\sigma}{d\Omega} = 1.55C^2S\sigma_{\text{DWUCK}}, \quad (1)$$

where C^2S is the spectroscopic factor for the transition and σ_{DWUCK} is the resultant DWBA differential cross section with the code DWUCK [19].

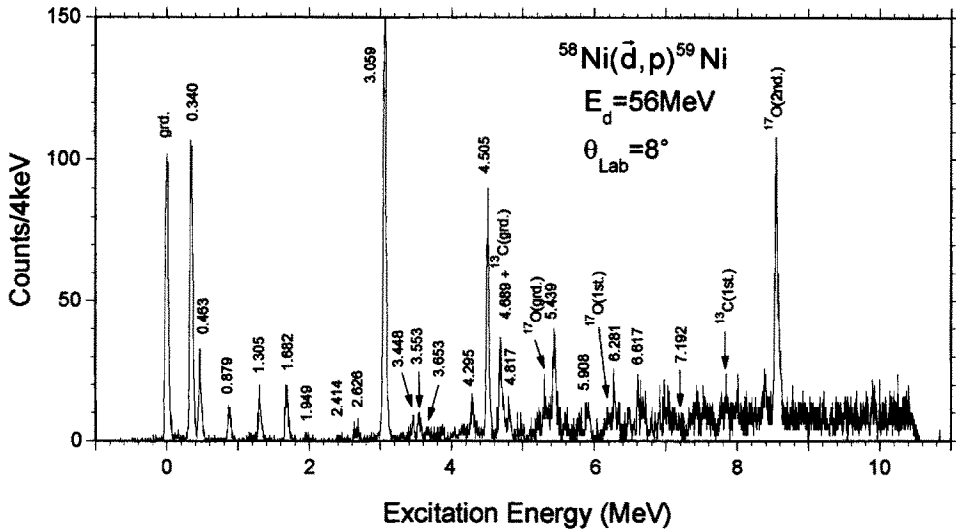


Fig. 1. Typical energy spectrum of protons from the $^{58}\text{Ni}(d, p)^{59}\text{Ni}$ reaction at 56 MeV for deuteron–spin up; $\theta_{\text{Lab}} = 8^\circ$.

| Polarized beam | | | | | | | | | | Unpolarized beam | | | | | |
|--------------------------------|-----|-----------------|--------|--------------------------------------|-----|-----------------|--------|---------------------------------------|-----|------------------|--------|--|-----|---------------|--------|
| $E_d = 56$ MeV Present work | | | | $E_d = 10$ MeV Aymar ^a | | | | $E_d = 10$ MeV Taylor ^b | | | | $E_d = 10$ MeV Chowdhury ^c | | | |
| E_x (MeV) | l | j | C^2S | E_x (MeV) | l | j | C^2S | E_x (MeV) | l | j | C^2S | E_x (MeV) | l | j | C^2S |
| 0.000 | 1 | $\frac{3}{2}$ | 0.537 | 0.000 | 1 | $\frac{3}{2}$ | 0.510 | 0.000 | 1 | $\frac{3}{2}$ | 0.530 | 0.000 | 1 | $\frac{3}{2}$ | 0.816 |
| 0.340 | 3 | $\frac{5}{2}$ | 0.687 | 0.341 | 3 | $\frac{5}{2}$ | 0.720 | 0.339 | 3 | $\frac{5}{2}$ | 0.480 | 0.340 | 3 | $\frac{5}{2}$ | 0.677 |
| 0.463 | 1 | $\frac{1}{2}$ | 0.538 | 0.465 | 1 | $\frac{1}{2}$ | 0.570 | 0.465 | 1 | $\frac{1}{2}$ | 0.440 | 0.465 | 1 | $\frac{1}{2}$ | 0.620 |
| 0.879 | 1 | $\frac{3}{2}$ | 0.073 | 0.879 | 1 | $\frac{3}{2}$ | 0.050 | 0.878 | 1 | $\frac{3}{2}$ | 0.063 | 0.881 | 1 | $\frac{3}{2}$ | 0.072 |
| 1.196 | (3) | $\frac{5}{2}$ | 0.015 | | | | | | | | | 1.191 | | n.s. | |
| 1.305 | 1 | $\frac{1}{2}$ | 0.339 | 1.303 | 1 | $\frac{1}{2}$ | 0.230 | 1.302 | 1 | $\frac{1}{2}$ | 0.210 | 1.298 | 1 | $\frac{1}{2}$ | 0.286 |
| 1.682 | 3 | $\frac{5}{2}$ | 0.104 | 1.686 | 3 | $\frac{5}{2}$ | 0.110 | 1.680 | 3 | $\frac{5}{2}$ | 0.060 | 1.683 | 3 | $\frac{5}{2}$ | 0.093 |
| | | | | | | | | 1.735 | 1 | $\frac{3}{2}$ | 0.008 | 1.733 | 1 | $\frac{3}{2}$ | 0.008 |
| 1.949 | 3 | $\frac{7}{2}$ | 0.012 | | | | | 1.948 | 3 | $\frac{7}{2}$ | 0.043 | 1.951 | 3 | $\frac{7}{2}$ | 0.037 |
| 2.414 | (1) | $\frac{3}{2}$ | 0.013 | | | | | | | | | 2.418 | 1 | $\frac{1}{2}$ | 0.016 |
| 2.626 | 3 | $\frac{7}{2}$ | 0.014 | | | | | | | | | 2.634 | 3 | $\frac{7}{2}$ | 0.079 |
| 2.685 | 3 | $\frac{5}{2}$ | 0.022 | | | | | | | | | 2.694 | 3 | $\frac{7}{2}$ | 0.023 |
| 3.059 | 4 | $\frac{9}{2}$ | 0.381 | 3.061 | 4 | $(\frac{9}{2})$ | 0.470 | 3.061 | 4 | $\frac{9}{2}$ | 0.560 | 3.060 | 4 | $\frac{9}{2}$ | 0.840 |
| 3.298 | | | | | | | | | | | | 3.317 ^d | | n.s. | |
| 3.448 | 1 | $\frac{3}{2}$ | 0.054 | 3.454 | 1 | $\frac{3}{2}$ | 0.031 | | | | | 3.460 | 1 | $\frac{1}{2}$ | 0.070 |
| 3.553 | 2 | $\frac{5}{2}$ | 0.019 | 3.538 | 2 | $(\frac{5}{2})$ | 0.023 | | | | | 3.542 | 2 | $\frac{5}{2}$ | 0.030 |
| 3.651 | 3 | $\frac{5}{2}$ | 0.021 | | | | | | | | | 3.648 | | n.s. | |
| 3.863 | 1 | $(\frac{3}{2})$ | 0.054 | | | | | 3.858 | 1 | $\frac{3}{2}$ | 0.018 | 3.865 | 1 | $\frac{1}{2}$ | 0.050 |
| 4.037 | 1 | $(\frac{3}{2})$ | 0.034 | | | | | | | | | 4.035 | 1 | $\frac{1}{2}$ | 0.024 |
| 4.160 | 1 | $(\frac{3}{2})$ | 0.068 | | | | | | | | | 4.155 | 1 | $\frac{1}{2}$ | 0.034 |
| 4.295 | (1) | $\frac{1}{2}$ | 0.109 | | | | | | | | | 4.262 | (1) | $\frac{1}{2}$ | 0.055 |
| | (4) | $\frac{9}{2}$ | 0.025 | | | | | | | | | 4.309 ^d | | n.s. | |
| 4.505 | 2 | $\frac{5}{2}$ | 0.154 | 4.495 | 2 | $\frac{5}{2}$ | 0.210 | 4.495 | 2 | $\frac{5}{2}$ | 0.120 | 4.504 | 2 | $\frac{5}{2}$ | 0.234 |
| 4.689 | 4 | $\frac{9}{2}$ | 0.037 | | | | | | | | | 4.695 | 4 | $\frac{9}{2}$ | 0.098 |
| 4.817 | 2 | $\frac{5}{2}$ | 0.033 | | | | | | | | | 4.805 | 2 | $\frac{5}{2}$ | 0.035 |
| 4.965 | 1 | $(\frac{3}{2})$ | 0.071 | | | | | | | | | 4.977 ^d | 1 | $\frac{1}{2}$ | 0.052 |
| 5.155 | 0 | $\frac{1}{2}$ | 0.124 | | | | | | | | | 5.150 | 0 | $\frac{1}{2}$ | 0.093 |
| 5.248 | 2 | $\frac{5}{2}$ | 0.017 | | | | | | | | | 5.213 | 2 | $\frac{5}{2}$ | 0.026 |
| 5.439 | | | | | | | | | | | | | | | |

Table 2 (continued)

| Polarized beam | | | | Unpolarized beam | | | |
|--------------------------------------|---------------------------------------|-----------------|--------|--|-----|---------------|--------|
| $E_d = 56$ MeV Present work | | | | $E_d = 10$ MeV Chowdhury ^c | | | |
| $E_d = 10$ MeV Aymar ^a | $E_d = 10$ MeV Taylor ^b | | | | | | |
| Ex (MeV) | l | j | C^2S | Ex (MeV) | l | j | C^2S |
| 6.375 | (0 | $\frac{1}{2}$) | 0.213 | 6.384 | 0 | $\frac{1}{2}$ | 0.078 |
| 6.467 | (2) | | | 6.512 | 2 | $\frac{5}{2}$ | 0.011 |
| 6.557 | | | | 6.582 ^d | | n.s. | |
| 6.617 | 2 | | | 6.650 | 2 | $\frac{5}{2}$ | 0.039 |
| 6.692 | (2) | | | 6.728 ^d | 2 | $\frac{5}{2}$ | 0.059 |
| 6.800 | (2) | | | 6.833 | 2 | $\frac{5}{2}$ | 0.009 |
| 6.909 | 2 | | | 6.942 ^d | 0 | $\frac{1}{2}$ | 0.052 |
| 7.014 | 2 | | | 7.032 ^d | 2 | $\frac{5}{2}$ | 0.024 |
| 7.116 | (2) | | | 7.163 | 0 | $\frac{1}{2}$ | 0.006 |
| 7.192 | (2) | | | 7.222 ^d | 2 | $\frac{5}{2}$ | 0.023 |
| 7.347 | 2 | $\frac{5}{2}$ | 0.044 | 7.388 ^d | 2 | $\frac{5}{2}$ | 0.017 |
| 7.427 | 2 | | | 7.443 ^d | 2 | $\frac{5}{2}$ | 0.020 |
| 7.533 | 2 | | | 7.597 ^d | 2 | $\frac{5}{2}$ | 0.031 |
| 7.623 | (2) | | | 7.669 ^d | 2 | $\frac{5}{2}$ | 0.011 |

^a Ref. [4].^b Ref. [5].^c Ref. [3].^d The excitation energy is averaged over several peaks of Ref. [3] within the resolution of the present experiment and the C^2S values are summed ones.

From the comparisons between experiment and theory, the transferred angular momenta l , j are assigned, and the spectroscopic factors are determined in the excitation energy region from 0 to 7 MeV. For almost all the strongly excited states, the diffraction patterns are clear to assign the l , j values. The consideration of the two-step process is important to analyze some excited states, which are excited via coupling with the surface vibration. In nickel isotopes, the coupling to the first excited 2^+ state in the target nucleus is remarkable. However, the effects of two-step processes become weaker in the transfer reaction as the incident energy increases up to the medium-energy region. Then only the one-step process is taken into account in the present analysis. The unbound single-particle states appearing above the excitation energy of 9.0 MeV were not analyzed in the present work.

3. Results

Fig. 1 shows a typical proton-energy spectrum from the $^{58}\text{Ni}(d, p)^{59}\text{Ni}$ reaction at 56 MeV in the excitation-energy region of 0–10 MeV at 8° laboratory angle. The

overall energy resolution was about 45 keV. Discrete levels are distributed throughout the excitation-energy region up to 7 MeV. Some strongly excited states are distributed in the excitation-energy region below 5 MeV. The number of weakly excited states increases at the excitation-energy region above 3 MeV. The spectrum data were analyzed with a peak-fitting and peeling-off program FO-

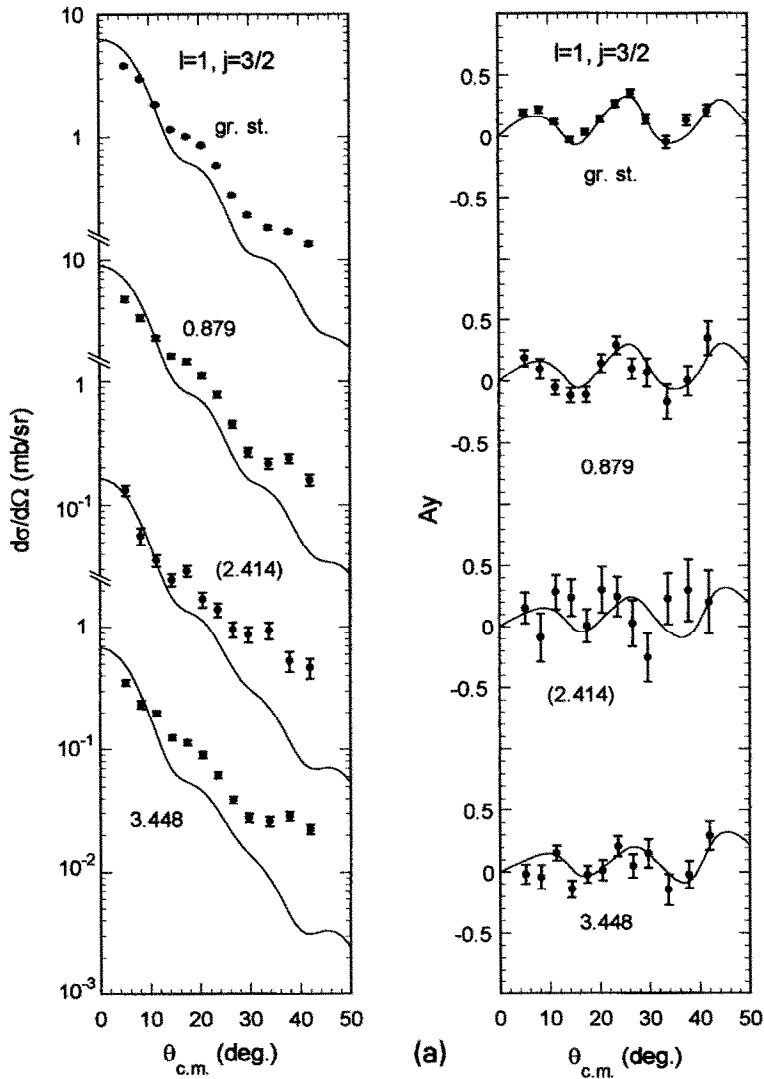


Fig. 2. Angular distributions of cross sections and analyzing powers for transitions to $2p_{3/2}$ states. Values in the figure show their excitation energies in MeV. Parentheses represent tentative spin assignments. Solid lines represent DWBA predictions, which are normalized to experiments.

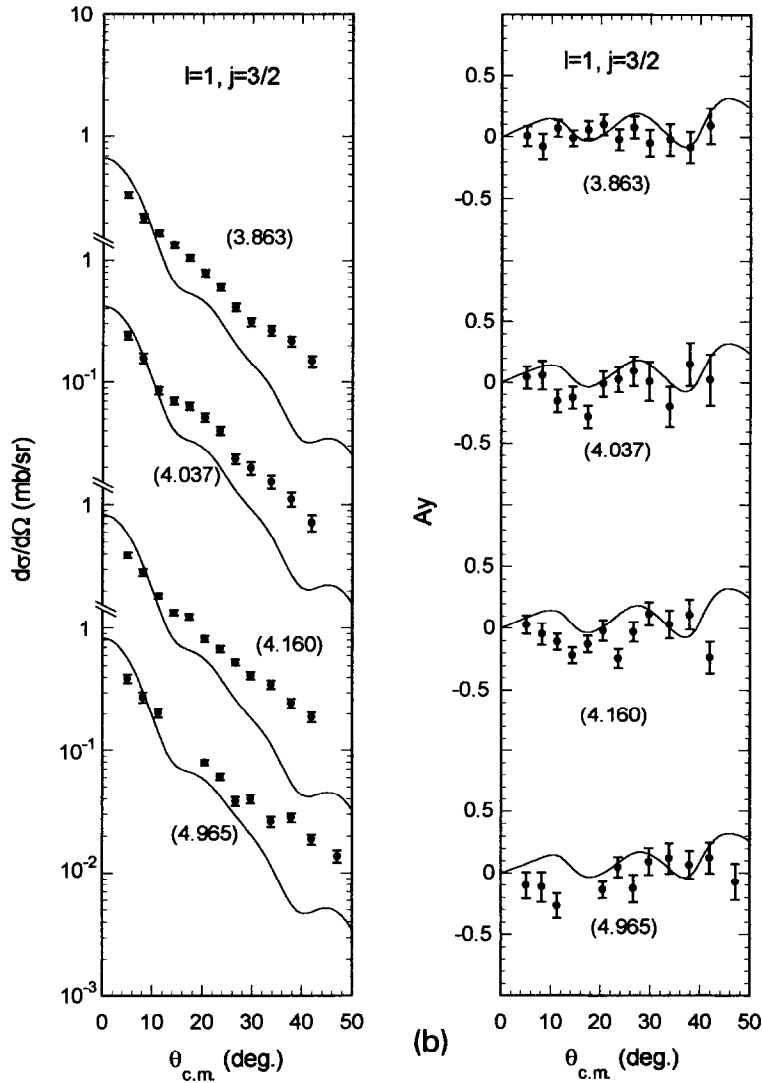


Fig. 2 (continued).

GRAS [23], which provided better data reduction for the complex peak spectra at the higher-excitation-energy region. Weak physical backgrounds are seen in the excitation-energy region higher than 6 MeV. Peaks located in the region higher than 8 MeV were not treated because of the difficulty of identification of the levels owing to the energy resolution in the present experiment.

The angular distributions of the cross sections and analyzing powers for the analyzed level are shown in Figs. 2–9 together with the DWBA predictions. The

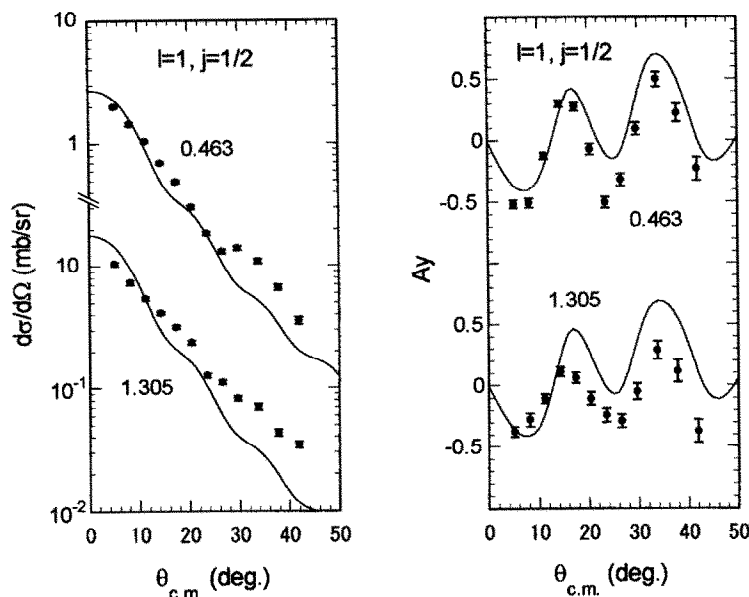


Fig. 3. Angular distributions of cross sections and analyzing powers for transitions to $2p_{1/2}$ states. Other notations are the same as Fig. 2.

transferred l, j values were assigned from the shape of the angular distribution. The angular distributions of the cross sections and analyzing powers for strongly excited states are in good agreement with the DWBA predictions in most cases. The assignments for the weakly excited states were performed by comparing with the cross section and analyzing power of the strongly excited states whose angular momenta are definitely assigned from the DWBA predictions. Fifty peaks were analyzed and 33 transitions were assigned the l, j values including 11 tentative assignments in the excitation-energy region below 8 MeV. The spectroscopic results are summarized in Table 2 together with the previous experimental results of Aymar et al. [4], Taylor et al. [5] and Chowdhury et al. [3]. Tentative spin assignments are in parentheses. The resultant assignments of l, j values are almost consistent with those in previous works except for some cases. Details of the results are discussed below.

(a) *The $l = 1$ transitions.* The angular distributions of the cross sections and analyzing powers for the $2p_{3/2}$ and $2p_{1/2}$ states are shown in Figs. 2 and 3, respectively. Almost all the strength of the $l = 1$ transferred states are observed at 0–1.3 MeV including the ground state. The angular distributions of the analyzing powers for these transitions are well reproduced by DWBA calculations. The angular distributions of the cross sections for these states exhibit the characteristic $l = 1$ transition, but DWBA calculations show a rather rapid decrease with increasing angles. Hence, the absolute value of the spectroscopic factors for the $l = 1$ transitions have some errors originated from the fitting of the experimental cross

sections to the DWBA predictions, which are considered as about 10%. The spectroscopic factors of these states are consistent with those of Aymar and Taylor. Ten weak $l = 1$ transitions are observed in the region of the excitation energy from 2.4 MeV to 6.1 MeV. The $j = 3/2$ assignment of Aymar et al. for the 3.448 MeV state is confirmed. For some of the other weakly excited states, the errors of the analyzing powers are large, so their spin assignments have been made tentatively.

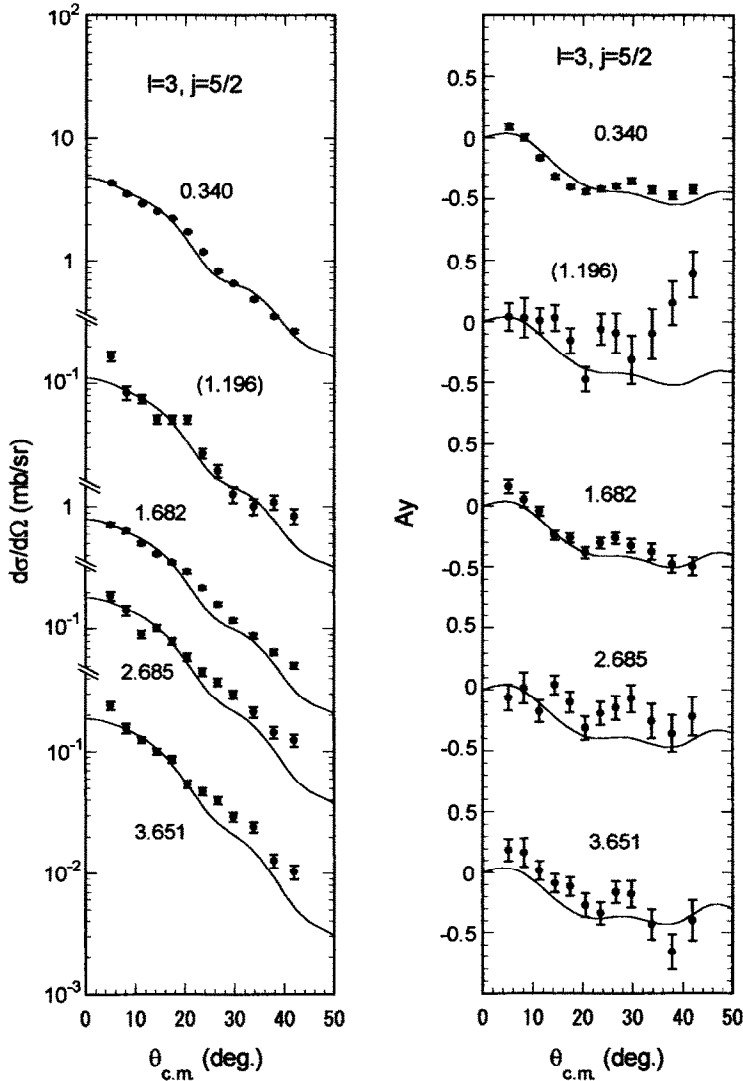


Fig. 4. Angular distributions of cross sections and analyzing powers for transitions to $1f_{5/2}$ states. Other notations are the same as Fig. 2.

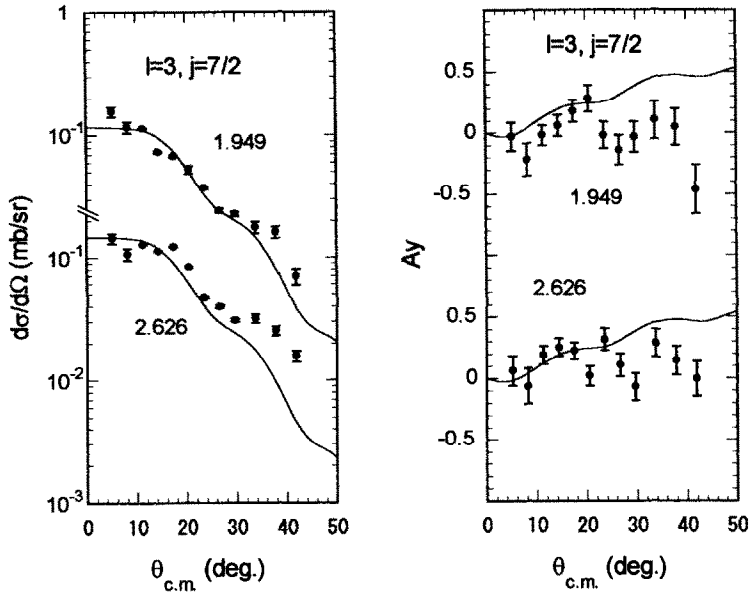


Fig. 5. Angular distributions of cross sections and analyzing powers for transitions to $1f_{7/2}$ states. Other notations are the same as Fig. 2.

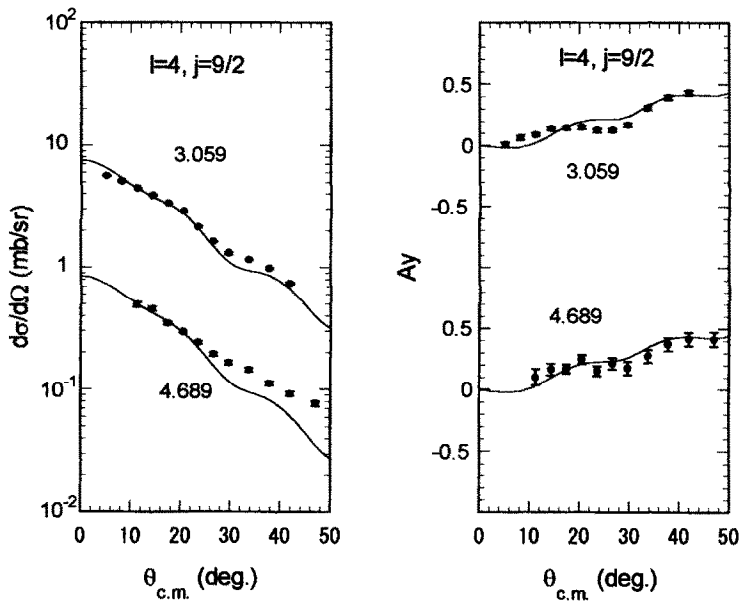


Fig. 6. Angular distributions of cross sections and analyzing powers for transitions to $1g_{9/2}$ states. Other notations are the same as Fig. 2.

(b) *The $l = 3$ transitions.* The $1f_{5/2}$ states at 0.340 and 1.682 MeV are strongly excited by the (d, p) reaction. Both the angular distributions of the cross sections and analyzing powers for these states are well reproduced by DWBA calculations as shown in Fig. 4. Some weak $l = 3$ transitions are observed at 1.9–3.7 MeV. The 2.685 and 3.651 MeV states are newly assigned as $1f_{5/2}$ states, which were explained as $j = 7/2$ and nonstripping states respectively from an unpolarized-beam experiment at $E_d = 10$ MeV by Chowdhury et al.. For 1.949 and 2.626 MeV

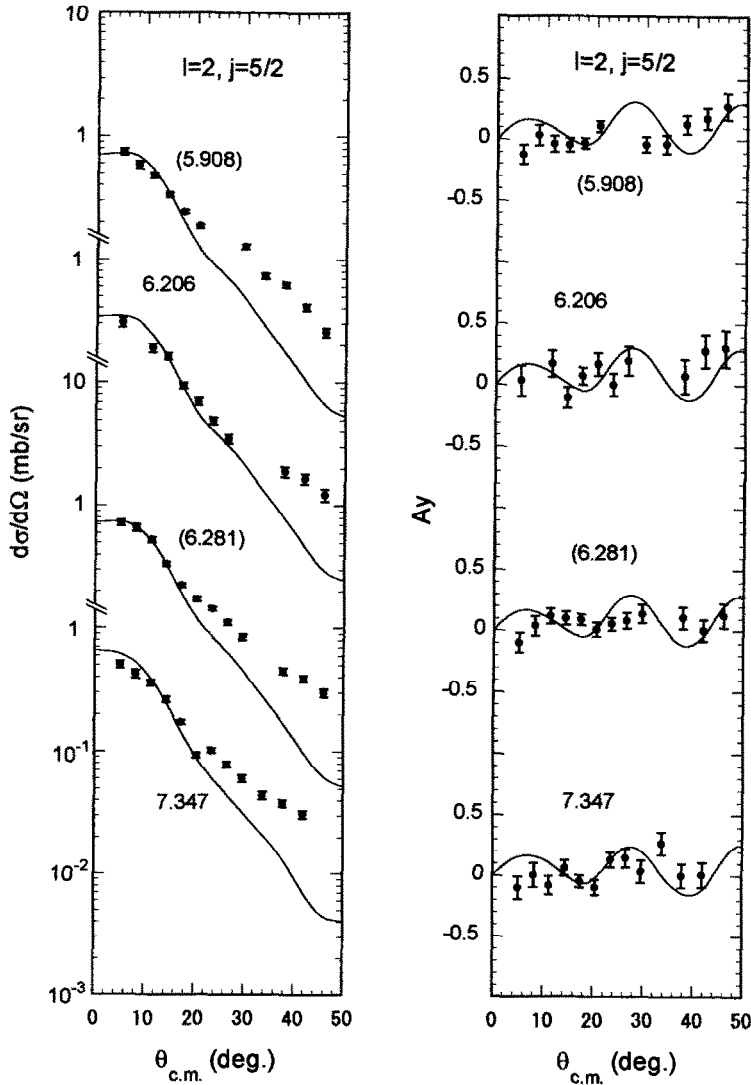


Fig. 7. Angular distributions of cross sections and analyzing powers for transitions to $2d_{5/2}$ states. Other notations are the same as Fig. 2.

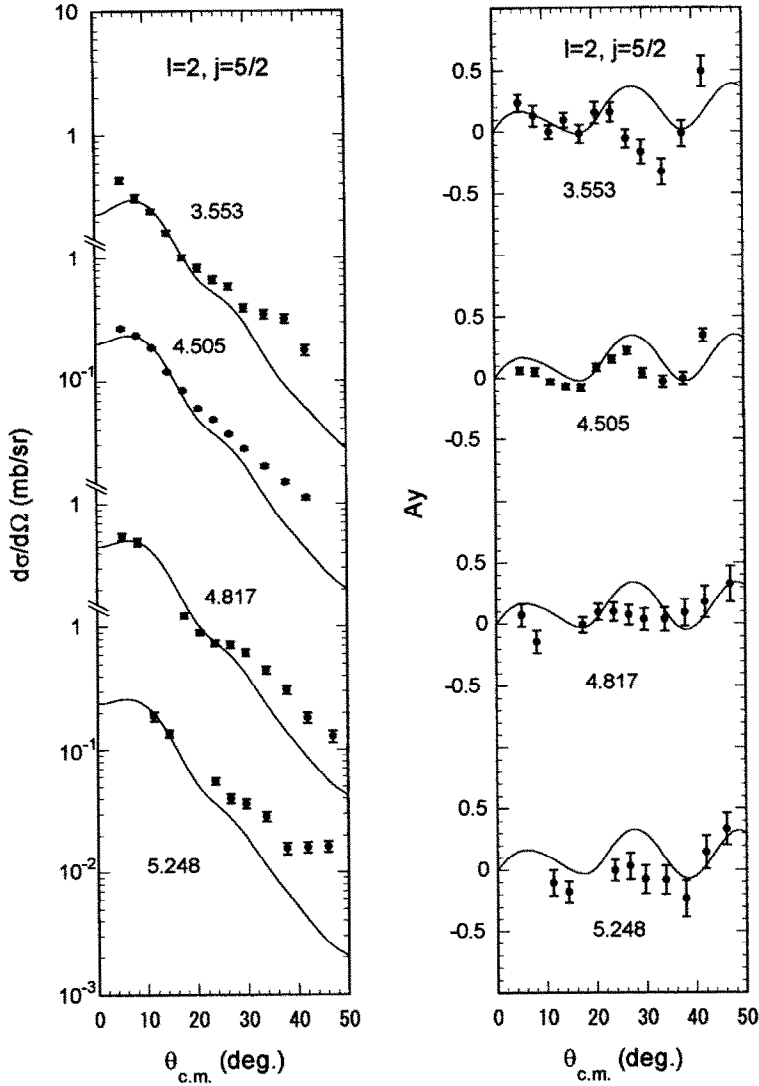


Fig. 7 (continued).

states confirmed as $1f_{7/2}$ states, the angular distributions of the analyzing powers, which have rather large errors, cannot be reproduced by the DWBA calculation at large angles (see Fig. 5), but they are clearly different from those of the $1f_{5/2}$ states. The weakly excited 1.196 MeV state, for which the angular distribution of the analyzing power shows a rather large deviation from the DWBA curve at large angles, is assigned as a $1f_{5/2}$ state tentatively. Nann et al. assigned the same j values for this state via the $^{60}\text{Ni}(p, d)^{59}\text{Ni}$ reaction [24]. They remarked on the

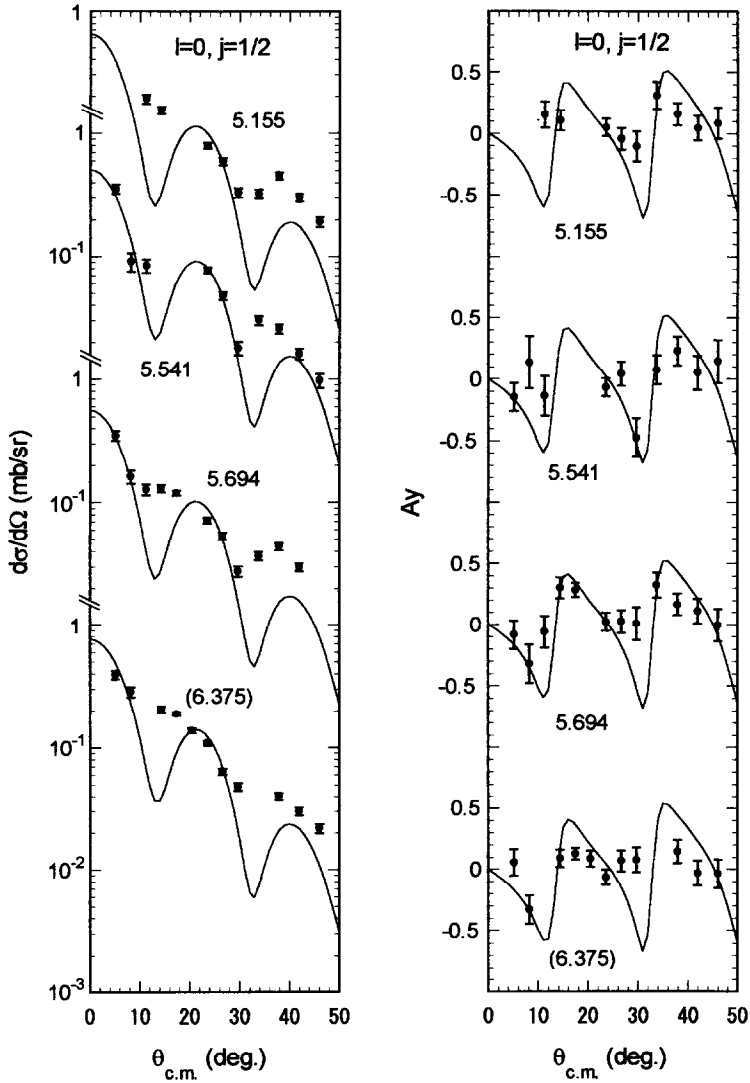


Fig. 8. Angular distributions of cross sections and analyzing powers for transitions to $3s_{1/2}$ states. Other notations are the same as Fig. 2.

possibility of the presence of the higher-order transfer-mechanism contribution to this state, since the angular distribution of the analyzing power for this state was different from the one for other $1f_{5/2}$ states in their work.

(c) *The $l = 4$ transitions.* Two transitions to the $1g_{9/2}$ states are observed at the excitation energies of 3.059 and 4.689 MeV. The angular distributions of the cross sections and analyzing powers are well reproduced with the DWBA calculation as shown in Fig. 6. At lower incident energy, the amplitude of diffraction of the

analyzing powers for $l = 4$ transitions are small as seen in the previous works of Aymar et al. and Taylor et al.. Then their assignments of j values have not been clear. The present work confirmed the assignments of these $1g_{9/2}$ states.

(d) *The $l = 2$ transitions.* The strongly excited $2d_{5/2}$ state is observed at 4.505 MeV, for which the angular distributions of the cross section and analyzing power exhibit good agreement with the DWBA predictions as shown in Fig. 7. For $l = 2$ excitations, the possibility of $1d$ states may be rejected from the shell-model systematics because the excitation of $1f_{7/2}$ states is quite weak. Weakly excited $l = 2$ states are observed at 3.5–7.6 MeV. For some of these highly excited states, j -assignments were not made because of their large error of analyzing powers and incompleteness of separation of complex peaks.

(e) *Other transitions.* Weak $l = 0$ transitions are observed at 5.1–6.4 MeV. The angular distributions of the cross sections and analyzing powers for these states are

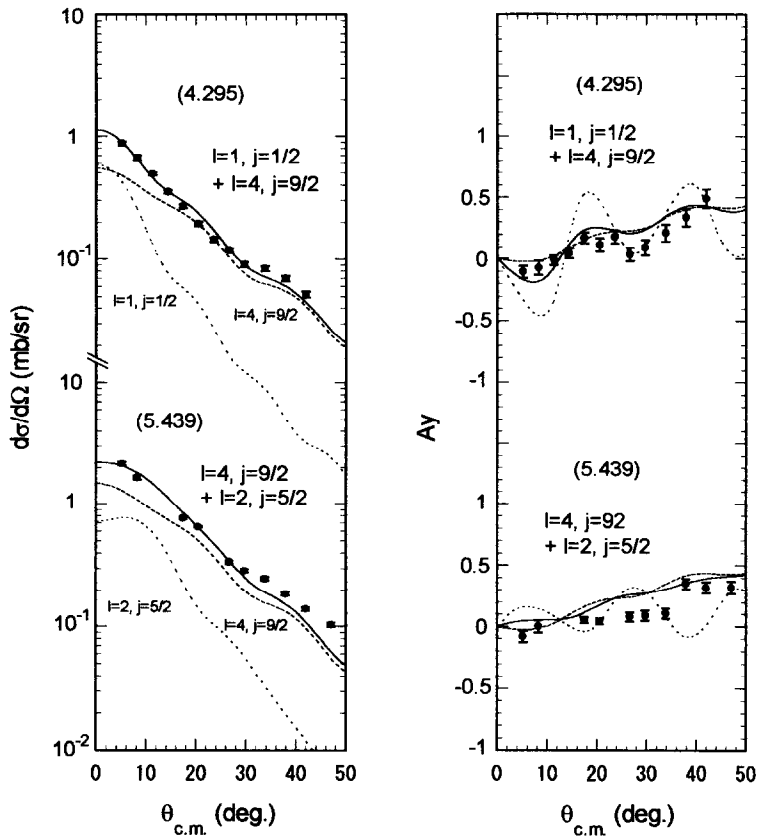


Fig. 9. Angular distributions of cross sections and analyzing powers for transitions to doublet states. The upper part is for the 4.395 MeV ($2p_{1/2} + 1g_{9/2}$) state and the lower part for the 5.439 MeV ($1g_{9/2} + 2d_{5/2}$) state, whose spin assignments are tentative. Solid lines show sums of DWBA calculations and broken lines show their components, which are normalized to reproduce experiments.

Table 3

The integrated properties of the neutron single-particle states observed in the present experiment

| Orbit | ΣC^2S | $\bar{E}_{x_{nlj}}$ (MeV) | Γ_{nlj} (MeV) |
|-----------|---------------|---------------------------|----------------------|
| $p_{3/2}$ | 0.664 (0.850) | 0.377 (1.170) | 2.24 (4.08) |
| $f_{5/2}$ | 0.834 (0.849) | 0.653 (0.662) | 1.74 (1.73) |
| $p_{1/2}$ | 0.877 (0.986) | 0.788 (1.176) | 0.96 (2.74) |
| $f_{7/2}$ | 0.026 (0.026) | 2.314 (2.314) | 0.79 (0.79) |
| $g_{9/2}$ | 0.418 (0.504) | 3.203 (3.528) | 1.09 (2.02) |
| $d_{5/2}$ | 0.290 (0.438) | 5.088 (5.325) | 2.59 (2.33) |
| $s_{1/2}$ | 0.360 (0.573) | 5.462 (5.801) | 0.54 (1.12) |

The data in parentheses show the quantities calculated including the spectroscopic factors for which spins are assigned tentatively.

shown in Fig. 8 together with the DWBA predictions for the $3s_{1/2}$ transfer. It may be ascribed to the closely-lying peaks that the minima of the cross sections of the DWBA predictions around 12° are not seen in the experimental cross sections. The 4.295 and 5.439 MeV states are regarded as doublets, which cannot be resolved experimentally. The assignments for these states were made by comparing

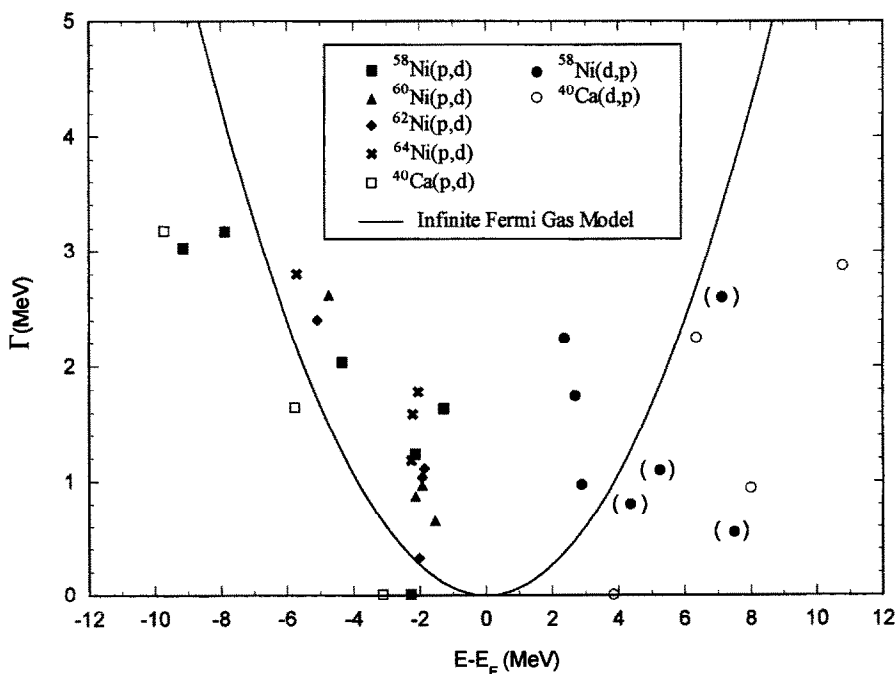


Fig. 10. Energy dependence of spreading widths for single-particle and -hole states evaluated from data of $^{58,60,62,64}\text{Ni}(p, d)$, $^{40}\text{Ca}(p, d)$, $^{58}\text{Ni}(d, p)$ and $^{40}\text{Ca}(d, p)$ reactions. The solid line represents a prediction of the infinite Fermi-gas model. Symbols in parentheses show orbits whose number of missing levels is considered to be large. Energy is scaled from the Fermi surface.

to the other strongly excited states, for which the angular distributions of the cross sections and analyzing powers were clearly obtained. Using obtained l, j values, spectroscopic factors were calculated to reproduce the experimental cross sections with DWBA predictions. The angular distributions of the cross sections and analyzing powers are shown in Fig. 9 together with the DWBA predictions and their component values.

4. Discussion

4.1. Single-particle states and spreading widths

Characteristics of single-particle states are often compared with theory in terms of integrated properties such as single-particle energies and spreading widths. The single-particle energy \bar{E}_{nlj} for the nlj state is obtained, in general, by calculating the center of gravity of the spectroscopic strength function or the spectroscopic factor $C^2S_{nlj}(E_i)$ as a function of energy, and the width Γ_{nlj} is obtained from the second moment of the spectroscopic strength function, which is regarded as the spreading width in the present work. The energy E_i for the i th level is related to the excitation energy Ex by the equation of

$$E_i = -S_n(^{59}\text{Ni}) + Ex, \quad (2)$$

where $S_n(^{59}\text{Ni})$ is the neutron-separation energy for ^{59}Ni . For the calculation of the single-particle energy and the spreading width, we used the equations of

$$\begin{aligned} \bar{E}_{nlj} &= \frac{\sum E_i C^2 S_{nlj}(E_i)}{\sum C^2 S_{nlj}(E_i)}, \\ \sigma_{nlj}^2 &= \frac{\sum (E_i - \bar{E}_{nlj})^2 C^2 S_{nlj}(E_i)}{\sum C^2 S_{nlj}(E_i)}, \\ \Gamma_{nlj} &= 2.35 \sigma_{nlj}, \end{aligned} \quad (3)$$

where Σ represents the sum over i . This single-particle energy \bar{E}_{nlj} is related to the averaged excitation energy $\bar{E}x_{nlj}$ by the equation of $\bar{E}_{nlj} = -S_n(^{59}\text{Ni}) + \bar{E}x_{nlj}$. In the present work, fragmentations of $2p_{3/2}$, $2p_{1/2}$, $1f_{5/2}$, $1g_{9/2}$ and $2d_{5/2}$ single-particle states are observed. The integrated properties for these states, which were calculated with the results in Table 2, are represented in Table 3. Values in parentheses in Table 3 show ones including tentatively assigned levels.

The energy dependence of spreading widths, which were calculated with the definitely assigned levels, are plotted in Fig. 10 together with spreading widths for both neutron-particle and -hole states in other Ni isotopes and ^{40}Ca obtained from previous experimental data with one-nucleon transfer reactions, $^{40}\text{Ca}(p, d)$ [9], $^{40}\text{Ca}(d, p)$ [25], $^{58-64}\text{Ni}(p, d)$ [26]. These spreading widths are plotted as a function of the energy differences from the Fermi surface: $\bar{E}_{nlj} - E_F$. In this work, the Fermi

energy was calculated from the mass-excess dependence [9,12], which is originally suggested by Jeukenne et al. [27]. The formula for the neutron Fermi energy of Jeukenne et al. was modified using the empirical mass formula [28]. The obtained Fermi-energy formula for the neutron is

$$E_F = -12.20 + 33.81\eta, \quad \eta = (N - Z)/A, \quad (4)$$

where N , Z and A are the neutron, proton and mass number of the target nucleus, respectively. The spreading widths located above the Fermi surface are for the single-particle states from the stripping reactions, and the spreading widths below the Fermi surface are for the single-hole states from pickup reactions. Symbols in parentheses in Fig. 10 show the results for which the number of missing levels is considered to be large. A prediction of the infinite Fermi-gas model is shown by a broken line that has a form

$$\Gamma = a|E - E_F|^2, \quad a = \frac{1}{15} (\text{MeV}^{-1}), \quad (5)$$

where E_F is the Fermi energy and a is a constant [29]. As a general trend, the spreading widths increase with increasing energy differences to the Fermi surface. This feature is in agreement with the infinite-model prediction. In details, the spreading widths for the Ni isotopes, however, do not vanish even very close to the Fermi surface for both single-particle and -hole states. The simple infinite-Fermi-gas-model prediction, which has a quadratic energy dependence, cannot reproduce the experimental spreading widths for Ni isotopes near the Fermi surface as shown by closed symbols in Fig. 10. On the other hand, values of the spreading widths for ^{40}Ca become zero near the Fermi surface for both single-particle and -hole states. The energy dependence for the doubly magic nucleus ^{40}Ca is clearly different from those for the Ni isotopes. This figure also represents the symmetrical behavior of spreading widths for single-particle and -hole states with respect to the Fermi surface though their energy dependences may depend on their own shell structures.

4.2. Neutron-bound-state complex potentials

In recent years, the dispersion-relation approaches to the optical-model potentials and the bound-state potentials have been studied for various nuclei. The bound-state potentials in the shell model are extrapolated from the optical potentials at the positive-energy region and then may have complex values [6]. The dispersion-relation approach is well adopted to interpret the Fermi-surface anomaly of the energy dependence of the volume integral of the real nucleon-optical potential [30]. Many of these approaches have been discussed about the doubly-magic nuclei, ^{208}Pb and ^{40}Ca . In the present work, the real and imaginary parts of the bound-state complex potentials are evaluated from experimental data of the single-particle energies and the spreading widths. We discuss the energy dependence of the neutron potential near the Fermi surface for the valence- and closed-shell nuclei, as for the Ni isotopes and ^{40}Ca .

The single-particle energies and spreading widths are related to the real and imaginary parts of the nucleon-bound-state potentials, respectively. The potential depths of the real and imaginary parts for the nlj state are calculated using a complex-potential-parameter search code CXBOUND [31] that solves the complex-eigenvalue equation,

$$\left(-\frac{\hbar^2}{2m} \frac{d^2}{dr^2} + \frac{\hbar^2}{2m} \frac{l(l+1)}{r^2} + V(r) + iW(r) + V_C(r) + V_{ls}(r)l \cdot s \right) u_{nlj}(r) = \left(E_{nlj} + \frac{i}{2} \Gamma_{nlj} \right) u_{nlj}(r), \quad (6)$$

where E_{nlj} and Γ_{nlj} are the single-particle (or -hole) energy and the spreading width for the nlj single-particle (or -hole) state, respectively; $V(r)$ and $W(r)$ are the real and imaginary parts of the nuclear potential respectively; $V_C(r)$ is the Coulomb potential; $V_{ls}(r)$ is the spin-orbit potential. The $u_{nlj}(r)$ is the single-particle radial wave function. This equation includes a general relation between the spreading width and the imaginary part of the bound-state potential in a constraint as

$$\Gamma_{nlj} = 2\langle W(r) \rangle, \quad (7)$$

where the bracket means the expectation value that is integrated with the single-particle wave function. The shapes of the potentials used were of usual optical-model potentials having the Woods–Saxon (volume) and the radial derivative Woods–Saxon (surface) forms. The volume-type contribution to the imaginary part was disregarded, since the volume-type contribution is negligible in this energy region near the Fermi surface. The geometrical parameters used were assumed to be constant, $r_0 = 1.25$ fm, $a_0 = 0.65$ fm, for all central potentials. Parameters for spin-orbit potentials were $V_{ls} = 6.0$ MeV, $r_{ls} = 1.25$ fm and $a_{ls} = 0.65$ fm. The Coulomb potential was generated by a uniform charge sphere of $r_C = 1.30$ fm. The potential depths of the real part of the volume type and the imaginary part of the surface type have been estimated for single-particle or -hole states used in the analysis.

The volume integral of the real and the imaginary parts of the neutron-bound-state potentials are plotted as a function of the energy difference from the Fermi surface in Fig. 11 (upper for real, lower for imaginary). The dotted lines in the upper part and in the lower part show the Hartree–Fock components of the real part and the imaginary part of the bound-state potential for the $^{58}\text{Ni} + n$ system, respectively, which have been obtained from the dispersion-relation approach for the $^{58}\text{Ni}(n, n)$ elastic-scattering cross sections at 1.5–24 MeV by Smith et al. [32]. The broken line and the solid line in the upper part show the Hartree–Fock component and the total value (Hartree–Fock + dispersion-relation contribution) of the real part, respectively, and the solid line in the lower part shows the imaginary part of the bound-state potential for the $^{40}\text{Ca} + n$ system, which is obtained from the dispersion-relation approach for the $^{40}\text{Ca}(n, n)$ elastic-scattering cross section at 5.3–40 MeV by Johnson et al. [33].

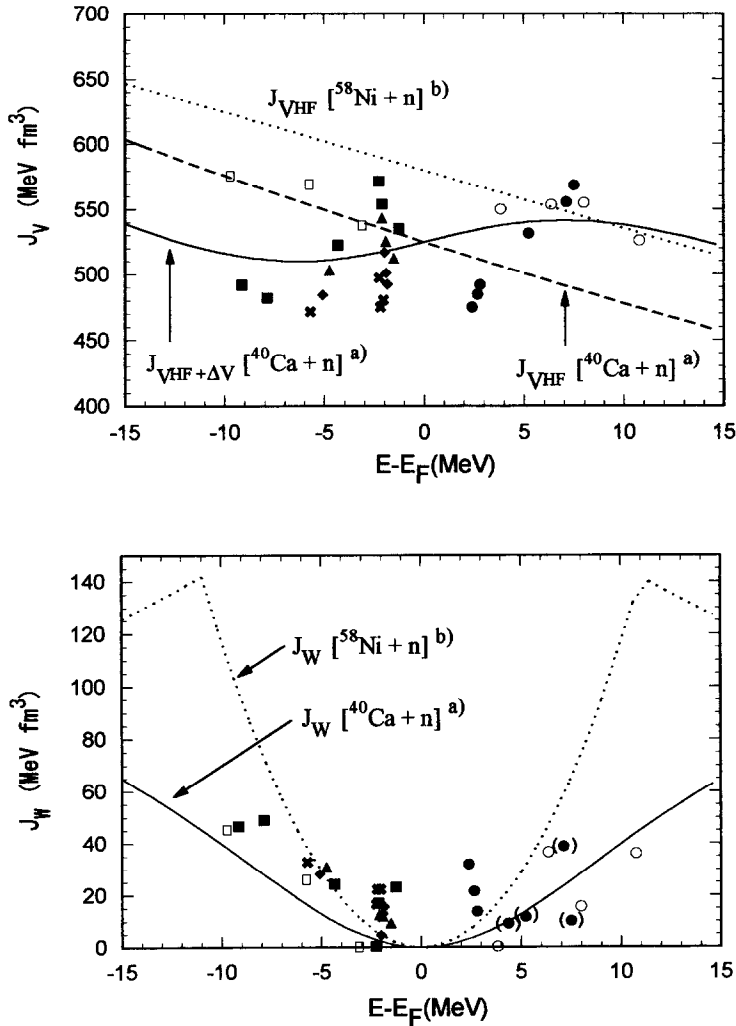


Fig. 11. Neutron-bound-state complex potentials evaluated from single-particle (or -hole) energies and spreading widths. The upper figure shows the energy dependence of volume integrals of real potentials, and the lower shows the energy dependence of volume integrals of imaginary potentials. The energy is scaled from the Fermi surface. J_{VHF} is the Hartree-Fock component of the real part of the optical potential, $J_{\Delta V}$ the volume integral of the dispersion-relation contribution to the real part, and J_W the volume integral of the imaginary part of the optical potential from Ref. [6] for (a) and Ref. [32] for (b).

The general tendency of both the real and imaginary parts of the bound-state potentials obtained from the data of stripping and pickup reactions are in agreement with those of the dispersion-relation approaches. The deviation of the real potential for the $^{58}\text{Ni} + n$ system is larger than that for the $^{40}\text{Ca} + n$ system. It is because the potential for the $^{40}\text{Ca} + n$ system has been constructed taking account

of the bound-state data but for the $^{58}\text{Ni} + n$ system. The total volume integral, $J_{V_{\text{HF}} + \Delta V}$, from the $^{40}\text{Ca} + n$ system is in good agreement with the ones obtained from the stripping- and pickup-reaction data on the average. The energy dependence of the imaginary parts is almost the same as of the spreading widths. The symmetric behaviors of the imaginary parts against the Fermi surface are also seen as in the spreading width. In comparison with the dispersive optical potentials, the imaginary parts for the Ni and Ca isotopes are in better agreement for the individual nucleus system. This feature shows that the imaginary parts of the bound-state potentials and of the optical potentials can be connected smoothly in each nucleus system. The obtained values are rather scattered and the estimations of their errors are considered to be difficult because of their complex contribution to the calculated results, so further discussions cannot be done at the present stage.

5. Conclusion

Angular distributions of the cross sections and analyzing powers were measured for the $^{58}\text{Ni}(d, p)^{59}\text{Ni}$ reaction up to the excitation energy of 10 MeV in ^{59}Ni with a polarized deuteron beam at 56 MeV. The spins and parities for 33 discrete levels were assigned and the spectroscopic factor for each state was obtained. The spins and parities for some states, for which some ambiguities have remained in the previous experiments, are confirmed and some are newly assigned. The single-particle energies and the spreading widths were obtained for $1f_{5/2}$, $2p_{3/2}$, $2p_{1/2}$, $1g_{9/2}$ states. Using these values, the neutron-bound-state complex potentials have been calculated together with results from other one-nucleon transfer reactions on Ni and Ca isotopes. It is found that the energy dependence of the spreading widths of the single-particle and -hole states and then the imaginary parts of the bound-state potentials show a symmetrical behavior with respect to the Fermi surface at the excitation energy below 10 MeV. The imaginary and real parts of the bound-state potentials are almost consistent with the optical potentials based on the dispersion relation.

We are grateful to the staff of the Research Center for Nuclear Physics, Osaka University, for the support of the experiments at the cyclotron facility. This work was performed at the RCNP under the program number 32A10.

References

- [1] R.H. Fulmer, A.L. McCarthy, B.L. Cohen and R. Middleton, Phys. Rev. 133 (1964) B955
- [2] E.R. Cosman, C.H. Paris, A. Sperduto and H.A. Enge, Phys. Rev. 142 (1966) 673
- [3] M.S. Chowdhury and H.M. Sen Gupta, Nucl. Phys. A205 (1973) 454
- [4] J.A. Aymar, H.R. Hiddleston, S.E. Darden and A.A. Rollefson, Nucl. Phys. A207 (1973) 596
- [5] T. Taylor and J.A. Cameron, Nucl. Phys. A337 (1980) 389
- [6] C. Mahaux and R. Sartor, Adv. Nucl. Phys. 20 (1991) 1, references on these topics are therein

- [7] M. Matoba, H. Ijiri, H. Kametani, T. Sakae, I. Kumabe, M. Hyakutake, N. Koori, T. Maki and T. Shiba, *Phys. Lett B*149 (1984) 50
- [8] M. Matoba, H. Ijiri, H. Kametani, I. Kumabe, M. Hyakutake, N. Koori, T. Sakae and T. Maki, *Nucl. Phys. A*456 (1986) 235
- [9] M. Matoba, H. Ijiri, H. Ohgaki, S. Uehara, T. Fujiki, Y. Uozumi, H. Kugimiya, N. Koori, I. Kumabe and M. Nakano, *Phys. Rev. C*39 (1989) 1658
- [10] M. Matoba, T. Sakae, Y. Uozumi, O. Iwamoto, K. Hisamochi, H. Ijiri, Y. Watanabe, N. Koori, T. Maki and M. Nakano, *J. Phys. Soc. Jpn.* 61 (1992) 3827
- [11] M. Matoba, O. Iwamoto, Y. Uozumi, T. Sakae, N. Koori, T. Fujiki, H. Ohgaki, H. Ijiri, T. Maki and M. Nakano, *Phys. Rev. C*48 (1993) 95
- [12] K. Hisamochi, O. Iwamoto, A. Kisanuki, S. Budihardjo, S. Widodo, A. Nohtomi, Y. Uozumi, T. Sakae, M. Matoba, M. Nakano, T. Maki, S. Matsuki and N. Koori, *Nucl. Phys. A*564 (1993) 227
- [13] G. Mairle, M. Seeger, M. Ermer, P. Grabmayr, A. Mondry and G.J. Wagner, *Phys. Rev. C*47 (1993) 2113
- [14] O. Iwamoto, R. Yamaguchi, A. Nohtomi, S. Widodo, M. Nakano, T. Maki, Y. Uozumi, T. Sakae and M. Matoba, 1991 RCNP annual report (1992) p. 17
- [15] Y. Uozumi, O. Iwamoto, A. Nohtomi, S. Widodo, T. Sakae, M. Matoba, M. Nakano and T. Maki, *Int. Nuclear Physics Conf. Wiesbaden* (1992)
- [16] H. Ikegami, S. Morinobu, I. Katayama, M. Fujiwara and S. Yamabe, *Nucl. Instr. Meth.* 175 (1980) 33
- [17] M. Matoba, K. Tsuji, K. Marubayashi, T. Shintake, H. Ikegami, T. Yamazaki, S. Morinobu, I. Katayama, M. Fujiwara and Y. Fujita, *Nucl. Instr. Meth.* 180 (1981) 419
- [18] N. Matsuoka, H. Sakai, T. Saito, K. Hosono, M. Kondo, H. Ito, K. Hatanaka, T. Ichihara, A. Okihana, K. Imai and K. Nisimura, *Nucl. Phys. A*445 (1986) 413
- [19] P.D. Kunz, code DWUCK, University of Colorado (unpublished)
- [20] G.R. Satchler, *Phys. Rev. C*4 (1971) 1485
- [21] F.D. Becchetti Jr. and G.W. Greenlees, *Phys. Rev.* 182 (1969) 1190
- [22] J.J.H. Menet, E.E. Gross, J.J. Malanify and A. Zucker, *Phys. Rev. C*4 (1971) 1114
- [23] S. Matsuki, code FOGRAS, Kyoto University, Chemical Research Institute (unpublished)
- [24] H. Nann, D.W. Miller, W.W. Jacobs, D.W. Devins, W.P. Jones and A.G.M. van Hees, *Phys. Rev. C*28 (1983) 642
- [25] Y. Uozumi et al., Kyushu University private communication, to be published in *Phys. Rev. C*
- [26] M. Matoba et al., Kyushu University private communication, to be published
- [27] J.-P. Jeukenne, C. Mahaux and R. Sartor, *Phys. Rev. C*43 (1991) 2211
- [28] W.D. Myers and W.J. Swiatecki, *Nucl. Phys.* 81 (1966) 1
- [29] G.F. Bertsch, P.F. Bortignon and R.A. Broglia, *Rev. Mod. Phys.* 55 (1983) 287
- [30] R.D. Lawson, P.T. Guenther and A.B. Smith, *Nucl. Phys. A*493 (1989) 267
- [31] Y.L. Luo and M. Kawai, code CXBOUND, Kyushu University private communication
- [32] A.B. Smith, P.T. Guenther, J.F. Whalen and S. Chiba, *J. Phys. G*18 (1992) 629
- [33] C.H. Johnson and C. Mahaux, *Phys. Rev. C*38 (1988) 2589